

Neutrino-nucleus coherent scattering as a probe of neutron density distributions

Kelly Patton^{1,*}, Jonathan Engel^{2,†}, Gail C. McLaughlin^{1,‡} and Nicolas Schunck^{3§}

¹*Physics Department, North Carolina State University, Raleigh, North Carolina 27695, USA*

²*Department of Physics and Astronomy, University of North Carolina, Chapel Hill, North Carolina 27599, USA*

³*Physics Division, Lawrence Livermore Laboratory, Livermore, California 94551 USA*

(Dated: July 4, 2012)

Neutrino-nucleus coherent elastic scattering provides a theoretically appealing way to measure the neutron part of nuclear form factors. Using an expansion of form factors into moments, we show that neutrinos from stopped pions can probe not only the second moment of the form factor (the neutron radius) but also the fourth moment. Using simple Monte Carlo techniques for argon, germanium, and xenon detectors of 3.5 tonnes, 1.5 tonnes, and 300 kg, respectively, we show that the neutron radii can be found with an uncertainty of a few percent when near a neutrino flux of 3×10^7 neutrinos/cm²/s. If the normalization of the neutrino flux is known independently, one can determine the moments accurately enough to discriminate among the predictions of various nuclear energy functionals.

PACS numbers: 25.30Pt

I. INTRODUCTION

The size of a nucleus is one of its most fundamental properties. Although the distributions of protons in nuclei are well known, the neutron distributions are comparatively poorly constrained. A precise measurement of neutron radii could have important implications in both nuclear physics and astrophysics.

In nuclear physics the most common framework for predicting neutron densities is energy density functional theory (DFT) — Skyrme or relativistic — with parameters that are at least in part fitted to other nuclear observables or pseudo-data such as nuclear-matter properties, root-mean-square radii, atomic masses, etc. [1]. Recent efforts to determine new generations of energy density functionals have pointed to the complex correlations among the values of physical quantities that they predict [2, 3]. Among observables used to optimize functionals, the neutron form factor is particularly important because it determines the neutron skin and radii, which in turn are strongly correlated in density functionals with the symmetry energy and incompressibility of nuclear matter [4]. Precise measurements of neutron radii could, therefore, significantly improve the predictive power of energy functionals.

In astrophysics, the size of the neutron skin may have important implications for neutron stars. While there are accurate measurements of pulsar orbital periods and masses, the radius of neutron stars, as well as their moments of inertia or gravitational redshift remain poorly constrained by observation, and must be provided by theory [5–8]. Such global properties as masses, radii, and composition, are determined by the equation of state

(EOS) of neutron-rich nuclear matter, which involves such quantities as the density dependence of the nuclear symmetry energy. As just noted, the symmetry energy is itself strongly correlated with the neutron skin [9]. Precise measurements on the neutron skin, therefore, provide information about the equation of state of neutron matter and thus the size of neutron stars [10].

Traditional measurements of neutron radii have involved hadronic scattering, with typical uncertainties of order 10%. Parity-violating electron scattering, used by the PREX experiment at Jefferson Laboratory to measure the radius of lead, is cleaner. The parity-violating asymmetry, i.e. the fractional difference in cross section between positive- and negative-helicity electrons, is roughly proportional to the weak form factor, which is the Fourier transform of the weak charge density. If one can measure the asymmetry (at a single Q^2) to 3% then one can determine the root mean square neutron radius to 1%. The uncertainty on the neutron radius from PREX is about 2.5% [11] but $\pm 1\%$ may be possible in the future.

The use of neutrino-nucleus coherent scattering to probe the weak form factor was first proposed in Ref. [12]. The authors considered a one tonne ⁴⁰Ar detector, with a nucleus described by a simplified form factor. Their analysis suggested that ton-scale detectors could replicate the 10% uncertainty of hadronic scattering methods when used in conjunction with a source of Michel-spectrum neutrinos. While large detectors are required since neutrinos interact only weakly, the theoretical interpretation of the results is straightforward and model independent. Neutrino-nucleus coherent scattering has been proposed for a number of other purposes as well, for example to detect supernova neutrinos [13], to measure the Weinberg angle [14, 15], to look for a neutrino magnetic moment, and to search for sterile neutrinos [16]. In all these cases, a weak nuclear form factor must be either measured or assumed before useful information can be extracted.

Both neutron and proton distributions in the nucleus

* kmpatton@ncsu.edu

† engelj@physics.unc.edu

‡ gail_mclaughlin@ncsu.edu

§ schunck1@llnl.gov

affect neutrino-nucleus coherent scattering, but the neutron distribution has much more leverage. In this paper we suggest the use of a Taylor expansion to write the nuclear-neutron form factor in terms of moments of the neutron density distribution. Using this expansion and a simple Monte Carlo simulation, we show that neutrino-nucleus coherent scattering can probe not only neutron radii, but also the higher-order moments of neutron distributions. We use the examples of argon [14], germanium [17] and xenon targets to show the expected ranges of sensitivity.

The paper is organized as follows. In section II, we introduce the model used to estimate neutrino-nucleus scattering count rates, including in our discussion the Taylor expansion of the neutron form factor and the calculation of the moments of the neutron distribution in nuclear DFT. In section III, we present and discuss the results of the Monte-Carlo simulations.

II. COHERENT SCATTERING AND THE FORM FACTOR

We present in this section the details of the model, including the kinematics of neutrino-nucleus coherent scattering, the dependence of the neutron form factor on the moments of the neutron distributions, and the DFT-based calculations of the moments.

A. Kinematics

To calculate the cross section for neutrino-nucleus coherent elastic scattering, we sum the contributions of each nucleon to the amplitude, which we then square and sum over available phase space. The resulting cross section, for spherical nuclei (neglecting small corrections from various sources) is [18]

$$\frac{d\sigma}{dT}(E, T) = \frac{G_F^2}{2\pi} M \left[2 - \frac{2T}{E} + \left(\frac{T}{E} \right)^2 - \frac{MT}{E^2} \right] \times \frac{Q_W^2}{4} F^2(Q^2), \quad (1)$$

where E is the energy of the incoming neutrino, T is the nuclear recoil energy, M is the mass of the nucleus, G_F is the Fermi constant, and $Q_W = N - (1 - 4\sin^2\theta_W)Z$ is the weak charge of the nucleus ($\sin^2\theta_W \approx 0.231$). The cross section also contains the form factor $F^2(Q^2)$, which is a function of the momentum transfer ($Q^2 = 2E^2TM/(E^2 - ET)$). One of the neglected corrections is from higher multipoles in odd-A nuclei, which include the effects of deformation as well as nonzero spin. The higher multipoles add terms to Eq. (1) only at order Q^4 , and even those changes are much smaller than $\mathcal{O}(1/A)$ for the nuclei considered here.

The form factor corrects for scattering that is not completely coherent at higher energies. It encodes information about the nuclear densities through a Fourier transform, which in spherical nuclei takes the approximate form [13]

$$F(Q^2) = \frac{1}{Q_W} \int [\rho_n(r) - (1 - 4\sin^2\theta_W)\rho_p(r)] \times \frac{\sin(Qr)}{Qr} r^2 dr, \quad (2)$$

where $\rho_{n,p}(r)$ are the neutron and proton densities. We have neglected effects due to the finite size of the nucleons, which alter the relation between the point-neutron density and the cross section by modifying the form factor at high Q . These effects could easily be included and would barely change the results of our sensitivity analysis below.

The separation of the neutron and proton terms in Eq. (2) makes it possible to write the form factor as

$$F(Q^2) = \frac{1}{Q_W} [F_n(Q^2) - (1 - 4\sin^2\theta_W)F_p(Q^2)]. \quad (3)$$

Since the coefficient of the proton form factor is small, the scattering depends mainly on the neutrons, making neutrino-nucleus coherent scattering well suited to measuring the neutron distribution.

There are two primary types of neutrino sources to consider: neutrinos generated from fission processes in nuclear reactors, and neutrinos from the decay of stopped pions. Reactor neutrinos have lower energy, resulting in correspondingly low nuclear-recoil energies. Because background can obscure low-energy recoil, we consider neutrinos produced from the decay of stopped pions. Stopped pions are produced in large quantities at both spallation sources and accelerator sources. An example of a spallation source is the Spallation Neutron Source at Oak Ridge National Laboratory, which hits a mercury target with a beam of protons. Pions are produced, with negative pions captured in the target and positive pions coming to rest and decaying. The pions decay through $\pi^+ \rightarrow \nu_\mu + \mu^+$. The muon neutrinos are monoenergetic with an energy of 29.9 MeV. The muons then come to rest and further decay via $\mu^+ \rightarrow e^+ + \nu_e + \bar{\nu}_\mu$. The probability that neutrinos ν_e or antineutrino $\bar{\nu}_\mu$ are emitted in the range $(E, E + dE)$ read

$$f_{\nu_e} = \frac{96}{m_\mu^4} (m_\mu E_{\nu_e}^2 - 2E_{\nu_e}^3) dE_{\nu_e},$$

$$f_{\bar{\nu}_\mu} = \frac{16}{m_\mu^4} (3m_\mu E_{\bar{\nu}_\mu}^2 - 4E_{\bar{\nu}_\mu}^3) dE_{\bar{\nu}_\mu}, \quad (4)$$

where m_μ is the mass of the muon. The energy of the neutrinos range up to ~ 52 MeV, which results in typical nuclear recoil energies on the order of tens of keV to 100 keV. The momentum transfer associated with these energies runs up to ~ 100 MeV.

To calculate the number of scattering events as a function of recoil energy, we fold the neutrino spectra with the cross section:

$$\frac{dN}{dT}(T) = N_t C \int_{E_{\min}(T)}^{m_\mu/2} f(E) \frac{d\sigma}{dT}(E, T) dE, \quad (5)$$

where N_t is the number of targets in the detector, C is the flux of neutrinos of a given flavor arriving at the detector, the normalized energy spectra $f(E)$ includes all three types of neutrino produced in pion decay, and $E_{\min}(T) = \frac{1}{2}(T + \sqrt{T^2 + 2TM})$ is the minimum energy a neutrino must have to cause a nuclear recoil at energy T . The upper bound of $m_\mu/2$ is the maximum energy for a neutrino produced from muon decay at rest.

B. Form-factor expansion

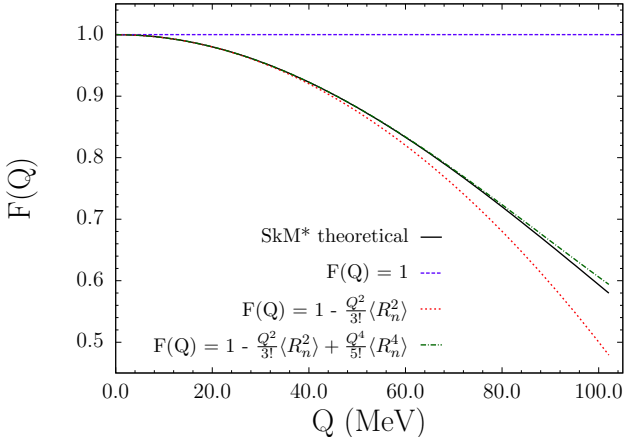


FIG. 1. (Color online.) The factor $F(Q^2)$ for ^{40}Ar predicted by the Skyrme functional SkM* (solid black curve), and truncations of the expanded form factor at various orders of Q : Q^0 (dashed blue curve), Q^2 (dashed red curve), Q^4 (solid green curve). Terminating the expansion at Q^4 (with coefficient $\frac{1}{5!}\langle R_n^4 \rangle$) gives good agreement with the full form factor over the range of Q^2 relevant for the scattering of neutrinos from stopped pion beams.

Since the form factor is included in the calculation of the number of events, nuclei with different density distributions will produce different recoil-energy distributions. The recoil distributions therefore provide a good test for models that predict the density. We can increase the usefulness of the recoil distribution by expanding the form factor in Q . The dominant neutron piece can be represented as

$$F_n(Q^2) \approx \int \rho_n(r) \left(1 - \frac{Q^2}{3!} r^2 + \frac{Q^4}{5!} r^4 - \frac{Q^6}{7!} r^6 + \dots \right) r^2 dr \\ \approx N \left(1 - \frac{Q^2}{3!} \langle R_n^2 \rangle + \frac{Q^4}{5!} \langle R_n^4 \rangle - \frac{Q^6}{7!} \langle R_n^6 \rangle + \dots \right) \quad (6)$$

with

$$\langle R_n^k \rangle = \frac{\int \rho_n r^k d^3r}{\int \rho_n d^3r}. \quad (7)$$

Written this way, the form factor is a sum of the even moments of the neutron density distribution. These moments are straightforward to calculate from the density, and represent physically relevant and measurable quantities. Since the neutrinos we consider have relatively low energy, we can truncate the expansion after just two terms for lighter nuclei such as argon and germanium, and three terms for heavier nuclei like xenon. As an illustration, we show in Fig. 1 the theoretical neutron form factor predicted by the Skyrme functional SkM* [19] for ^{40}Ar . Including moments up to $\langle R_n^4 \rangle$ is sufficient to reproduce the full form factor curve over the relevant range of Q values. In other words, we can fit experimental scattering data in ^{40}Ar with just two parameters, $\langle R_n^2 \rangle$ and $\langle R_n^4 \rangle$.

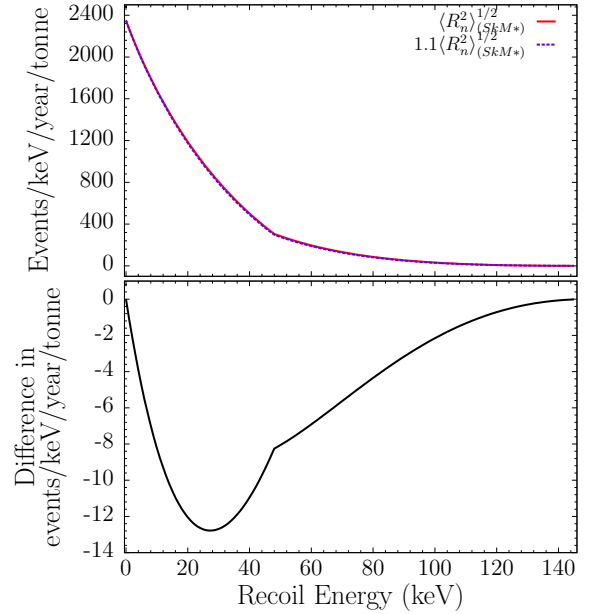


FIG. 2. (Color online.) Top: Event rates in ^{40}Ar as a function of recoil energy, with two different RMS neutron radii. The red (solid) curve represents predictions of the Skyrme functional SkM*, while the blue (dotted) curve represents the same for an RMS radius made 10% larger, as described in the text. The flux at the detector is taken to be 3×10^7 neutrinos/cm²/sec per flavor. Bottom: The difference between the two curves on top.

Fig. 2 shows the effects on event rates in ^{40}Ar of changing a single important measure of the density distribution, the root-mean-square (RMS) neutron radius $\langle R_n^2 \rangle^{\frac{1}{2}}$. We produced the figure as follows: First, we calculated

TABLE I. Isotopes and abundances used in the calculations for germanium and xenon [22].

Isotope	Abundance	Isotope	Abundance
^{70}Ge	0.205	^{128}Xe	0.0191
^{72}Ge	0.274	^{129}Xe	0.264
^{73}Ge	0.078	^{130}Xe	0.041
^{74}Ge	0.365	^{131}Xe	0.212
^{76}Ge	0.078	^{132}Xe	0.269
		^{134}Xe	0.104
		^{136}Xe	0.089

event rates as a function of recoil energy with the functional SkM*, via the expansion in Eq. (6). Next, we did the same with the RMS neutron radius 10% larger and no changes to the other terms in the expansion. The resulting curves for ^{40}Ar , with an assumed neutrino flux of 3×10^7 neutrinos/cm²/sec per flavor, appear in the upper panel of Fig. 2, while the difference between them is plotted in the bottom panel. A 10% difference in the RMS neutron radius results in a difference of ~ 780 events/tonne/year, which is about 1.2% of the total event rate over the entire energy range. This difference is concentrated at a nuclear recoil energy of 30 keV.

We obtain similar results in Ge and Xe, though there we must use effective moments, which we define in the next section, to average over different isotopes. In Ge, a 10% difference in the effective RMS radius yields an integrated difference of ~ 8100 events/tonne/year, or about 6% of the total, concentrated around a nuclear recoil of 15 keV. In Xe the same change in effective RMS radius results in a difference of ~ 20200 events/tonne/year, or about 8% of the total, and is concentrated at a nuclear recoil energy of 8 keV.

As Q^2 goes to zero, the form factor approaches $F(0) = 1$, so the low energy portions of the event-rate curves converge and all the difference curves go to zero. At high energies, there are very few events, so both event-rate curves approach zero and the differences also approach zero. The larger elements have smaller total recoil-energy ranges. In all three cases, however, the largest difference in the event-rate curves occurs at a recoil energy of about 20% of the maximum. We note that the high-

est and lowest energies will most likely be excluded from an experimental analysis because of background at the detector, and that the effect of changing $\langle R_n^2 \rangle^{\frac{1}{2}}$ is most prominent in the energy range that is experimentally accessible to cryogenic detectors such as CLEAN [20] and CLEAR [14, 21], even though more events occur at inaccessibly low recoil.

C. Effective Moments

Naturally occurring argon is made at 99.6% of ^{40}Ar : the expansion in Eq. (6) is therefore sufficient to accurately compute neutrino-nucleus scattering. Germanium and xenon, however, both have multiple isotopes that occur naturally with relatively high abundance (see table I). To account for that fact, we define effective moments for these elements as follows:

To calculate the event curves for germanium and xenon, it is necessary to sum over all isotopes. There are several isotope-specific quantities in the cross section, including the mass, neutron number, and the moments of the neutron and proton distributions. In addition, each isotope will have a different number of atoms in the detector. To calculate the rate for all isotopes, we therefore use

$$\frac{dN}{dT}(T) = N_A M_{\text{detector}} C \times \int f(E) \sum_i \left[\frac{X_i}{M_i} \left(\frac{d\sigma}{dT}(T, E) \right)_i \right] dE, \quad (8)$$

where the coefficient N_t in Eq. (5) is now replaced by $N_A M_{\text{detector}}$ and a summation over isotopes i of the cross-section with the weights X_i/M_i . Here, X_i is the natural abundance of isotope i , M_i is the mass of that isotope, N_A is Avogadro's number, and M_{detector} is the total mass of the element (including all its isotopes) in the detector.

Since the form factor appears squared in the cross section, the sum in Eq. (8) will have neutron terms, proton terms, and terms that include both neutron and proton moments (see Eq. (3)). The definitions for the proton effective moments will follow the same pattern as those for the neutrons, so we will concentrate only on the neutrons at this point.

Some algebra and the definitions of the cross section and form factor allow us to write the sum in Eq. (8) as

$$\begin{aligned}
\sum_i \left[\frac{X_i}{M_i} \left(\frac{d\sigma}{dT}(T, E) \right)_i \right] &= \frac{G_F^2}{8\pi} \left[\sum_i (X_i N_i^2) \left(2 - \frac{2T}{E} + \left(\frac{T}{E} \right)^2 \right) - \sum_i (X_i N_i^2 M_i) \left(\frac{T}{E^2} \right) \right. \\
&\quad - \sum_i (X_i N_i^2 M_i \langle R_n^2 \rangle_i) \left(2 - \frac{2T}{E} + \left(\frac{T}{E} \right)^2 \right) \frac{Q^2}{3\langle M \rangle} + \sum_i (X_i N_i^2 M_i^2 \langle R_n^2 \rangle_i) \left(\frac{T}{E^2} \right) \frac{Q^2}{3\langle M \rangle} \\
&\quad + \sum_i (X_i N_i^2 M_i^2 \langle R_n^2 \rangle_i^2) \left(2 - \frac{2T}{E} + \left(\frac{T}{E} \right)^2 \right) \frac{Q^4}{36\langle M \rangle^2} - \sum_i (X_i N_i^2 M_i^3 \langle R_n^2 \rangle_i) \left(\frac{T}{E^2} \right) \frac{Q^4}{36\langle M \rangle^2} \\
&\quad + \sum_i (X_i N_i^2 M_i^2 \langle R_n^4 \rangle_i) \left(2 - \frac{2T}{E} + \left(\frac{T}{E} \right)^2 \right) \frac{Q^4}{60\langle M \rangle^2} - \sum_i (X_i N_i^2 M_i^3 \langle R_n^4 \rangle_i) \left(\frac{T}{E^2} \right) \frac{Q^4}{60\langle M \rangle^2} \\
&\quad - \sum_i (X_i N_i^2 M_i^3 \langle R_n^2 \rangle_i \langle R_n^4 \rangle_i) \left(2 - \frac{2T}{E} + \left(\frac{T}{E} \right)^2 \right) \frac{Q^6}{360\langle M \rangle^3} \\
&\quad \left. - \sum_i (X_i N_i^2 M_i^4 \langle R_n^2 \rangle_i \langle R_n^4 \rangle_i) \left(\frac{T}{E^2} \right) \frac{Q^6}{360\langle M \rangle^3} + \dots \right], \tag{9}
\end{aligned}$$

where $\langle M \rangle = \sum_i X_i M_i$ and $Q^2 = 2E^2 T \langle M \rangle / (E^2 - ET)$. In the above equation, we have kept all terms that have $\langle R_n^2 \rangle$, $\langle R_n^4 \rangle$, or both. (For xenon, we use all additional terms that include $\langle R_n^6 \rangle$.) In this expression several effective (isotope-weighted) moments occur, two of each order. The two effective second moments, after normalization, are

$$\langle R_n^2 \rangle_{\text{eff},1} = \frac{\sum_i X_i N_i^2 M_i \langle R_n^2 \rangle_i}{\sum_i X_i N_i^2 M_i}, \tag{10}$$

$$\langle R_n^2 \rangle_{\text{eff},2} = \frac{\sum_i X_i N_i^2 M_i^2 \langle R_n^2 \rangle_i}{\sum_i X_i N_i^2 M_i^2}, \tag{11}$$

and the two effective fourth moments are

$$\langle R_n^4 \rangle_{\text{eff},1} = \frac{\sum_i X_i N_i^2 M_i^2 \langle R_n^4 \rangle_i}{\sum_i X_i N_i^2 M_i^2}, \tag{12}$$

$$\langle R_n^4 \rangle_{\text{eff},2} = \frac{\sum_i X_i N_i^2 M_i^3 \langle R_n^4 \rangle_i}{\sum_i X_i N_i^2 M_i^3}. \tag{13}$$

The differences between the values of the two moments of each order is small, as can be seen for the Skyrme functional SkM* in table II. In fact, these differences are smaller than the typical numerical uncertainties in DFT calculations coming from the truncation of the basis or the size of the mesh. We therefore make the approximation that the two second moments are equal (calling them $\langle R_n^2 \rangle_{\text{eff}}$) and that the two fourth moments are equal (calling them $\langle R_n^4 \rangle_{\text{eff}}$). There are also terms in the cross section that involve $\langle R_n^2 \rangle^2$, from which we can define $(\langle R_n^2 \rangle^2)_{\text{eff}}$. Although mathematically $(\langle R_n^2 \rangle^2)_{\text{eff}}$ is not equal to $(\langle R_n^2 \rangle_{\text{eff}})^2$, numerically they are very similar, as shown in table II. After equating them and making the similar approximations just described, we can rewrite Eq. 9 in terms of effective moments as

$$\begin{aligned}
\sum_i \left[\frac{X_i}{M_i} \left(\frac{d\sigma}{dT}(T, E) \right)_i \right] = & \frac{G_F^2}{8\pi} \left[\sum_i (X_i N_i^2) \left(2 - \frac{2T}{E} + \left(\frac{T}{E} \right)^2 \right) - \sum_i (X_i N_i^2 M_i) \left(\frac{T}{E^2} \right) \right. \\
& - \langle R_n^2 \rangle_{\text{eff}} \sum_i (X_i N_i^2 M_i) \left(2 - \frac{2T}{E} + \left(\frac{T}{E} \right)^2 \right) \frac{Q^2}{3\langle M \rangle} + \langle R_n^2 \rangle_{\text{eff}} \sum_i (X_i N_i^2 M_i^2) \left(\frac{T}{E^2} \right) \frac{Q^2}{3\langle M \rangle} \\
& + \langle R_n^2 \rangle_{\text{eff}}^2 \sum_i (X_i N_i^2 M_i^2) \left(2 - \frac{2T}{E} + \left(\frac{T}{E} \right)^2 \right) \frac{Q^4}{36\langle M \rangle^2} - \langle R_n^2 \rangle_{\text{eff}}^2 \sum_i (X_i N_i^2 M_i^3) \left(\frac{T}{E^2} \right) \frac{Q^4}{36\langle M \rangle^2} \\
& + \langle R_n^4 \rangle_{\text{eff}} \sum_i (X_i N_i^2 M_i^2) \left(2 - \frac{2T}{E} + \left(\frac{T}{E} \right)^2 \right) \frac{Q^4}{60\langle M \rangle^2} - \langle R_n^4 \rangle_{\text{eff}} \sum_i (X_i N_i^2 M_i^3) \left(\frac{T}{E^2} \right) \frac{Q^4}{60\langle M \rangle^2} \\
& - \langle R_n^2 \rangle_{\text{eff}} \langle R_n^4 \rangle_{\text{eff}} \sum_i (X_i N_i^2 M_i^3) \left(2 - \frac{2T}{E} + \left(\frac{T}{E} \right)^2 \right) \frac{Q^6}{360\langle M \rangle^3} \\
& \left. + \langle R_n^2 \rangle_{\text{eff}} \langle R_n^4 \rangle_{\text{eff}} \sum_i (X_i N_i^2 M_i^4) \left(\frac{T}{E^2} \right) \frac{Q^6}{360\langle M \rangle^3} + \dots \right], \tag{14}
\end{aligned}$$

TABLE II. Numerical values for the different effective moments of germanium and xenon as well as the percent difference between definitions. The definitions for the effective moments are given in equations 10-13. The values of $(\langle R_n^2 \rangle_{\text{eff}})^{1/4}$ are compared to those of $\langle R_n^2 \rangle_{\text{eff},1}^{1/2}$.

	Ge	Xe
$\langle R_n^2 \rangle_{\text{eff},1}^{1/2}$ (fm)	4.0495	4.8664
$\langle R_n^2 \rangle_{\text{eff},2}^{1/2}$ (fm)	4.0505	4.8668
% Difference	0.02	0.009
$\langle R_n^4 \rangle_{\text{eff},1}^{1/4}$ (fm)	4.3765	5.2064
$\langle R_n^4 \rangle_{\text{eff},2}^{1/4}$ (fm)	4.3774	5.2068
% Difference	0.02	0.009
$(\langle R_n^2 \rangle_{\text{eff}})^{1/4}$ (fm)	4.0509	4.8670
% Difference	0.001	0.01

The approximations leading to Eq. (14) from Eq. (9) cause an error of 0.01% over the entire event curve.

We define effective moments for the protons in the same way as for neutrons. The terms in the cross section that involve both neutron moments and proton moments can be calculated from these effective moments. Since the proton moments are known quite accurately from electron scattering, we are finally able to represent the recoil distribution in terms of just two unknown parameters, $\langle R_n^2 \rangle_{\text{eff}}$ and $\langle R_n^4 \rangle_{\text{eff}}$, or three for xenon.

D. Density Functional Theory Calculations of Moments

Our Monte-Carlo simulations require the knowledge of the radii and moments $\langle R_{n,p}^k \rangle$ of the neutron and proton distributions in both even-even and odd-even isotopes.

In this work, we compute these quantities in DFT with Skyrme functionals. We use nine common parameterizations of the Skyrme functional (SkM* [19], SkI3 [23], SLy4 [24], SLy5 [24], SkX [25], HFB9 [26], SkO [27], UNEDF0 [2] and UNEDF1 [3]). These functionals are characterized by relatively different nuclear matter, surface, and deformation properties, and therefore provide a good “statistical” sample of Skyrme functionals.

We model pairing correlations with a density-dependent delta pairing force with mixed volume-surface characteristics and the Lipkin-Nogami prescription to approximate particle number projection. For each element, we fit the strength of the pairing force to odd-even mass differences according to the general procedure outlined in [2]: in ^{40}Ar for argon, ^{72}Ge for germanium and ^{130}Xe for xenon. Only parameterizations UNEDF0 and UNEDF1 are accompanied by specific prescriptions for the pairing channel. We compute the ground-state in odd-mass isotopes by performing systematic blocking calculations: for a given odd-mass isotope, we consider all blocking configurations within 2 MeV of the ground state of the neighboring even-even nucleus, and take the ground state of the odd isotope to be the configuration yielding the lowest energy with the correct spin.

We carry out all these calculations with the latest version of the DFT solver HFBTHO [28]. The code solves the Skyrme Hartree-Fock-Bogoliubov equations in a harmonic oscillator basis with axial symmetry and, therefore, time-reversal invariance. We perform all calculations in a full HO basis of 20 shells with a basis frequency parameter defined by $\hbar\omega = 1.2 \times 41/A^{1/3}$. In argon and germanium isotopes the basis is spherical, while in xenon isotopes, the ground states of which are weakly deformed, its deformation is $\beta_2 = 0.3$. Such characteristics ensure excellent convergence of the results [29]. We do the blocking calculations in the equal filling approximation [30], which agrees with the full blocking prescription to within 100 keV or less [31].

III. RESULTS AND DISCUSSION

A. Monte-Carlo simulations

We use a simple Monte Carlo simulation to give an idea of how accurately the nuclear moments can be determined. We assume that a detector, filled with either ^{40}Ar , natural germanium, or natural xenon, experiences a flux from the decay of pions at rest of 3×10^7 neutrinos/cm²/sec in each flavor for one year. The neutrino production rate at the Spallation Neutron Source at Oak Ridge National Laboratory [14], DAE δ ALUS [32, 33] and the European Spallation Source [34] ranges from 1×10^{15} neutrinos/sec to 3.5×10^{15} neutrinos/sec of each flavor. A flux of 3×10^7 neutrinos/cm²/sec corresponds to detectors placed approximately 16 m from the source at SNS, 18 m from the source at DAE δ ALUS, and 30 m from the source at ESS.

We perform a Monte Carlo simulation that includes statistical error and uncertainty on the beam normalization. Another significant source of systematic error is the uncertainty in the detection efficiency. We discuss this in Sec. III B, and for the purposes of the Monte Carlo assume 100% detection efficiency. We also assume that leptons and photons produced by charge-current and inelastic neutral-current scattering can be detected and the corresponding events efficiently rejected as background.

We calculate a recoil curve assuming that the true nuclear density distributions are given by the Skyrme model SkM*. We place the events into bins based on energy, and then add Gaussian-distributed statistical noise to each bin. We then take the general form factor from Eq. 14 and use χ^2 minimization to find the optimal values of $\langle R_n^2 \rangle$, $\langle R_n^4 \rangle$, or the effective moments, and the beam normalization. In the case of xenon, we use the same procedure to find the optimal value of $\langle R_n^6 \rangle$. Typical values of χ^2 range from 0.5 to 10.

We do separate sets of runs, some assuming that the normalization of the flux is determined by other means, and some allowing for an uncertainty of $\pm 10\%$ in the normalization. Because background is anticipated to be substantial at high and low energies, we exclude the highest and lowest bins from the χ^2 minimization. The energy ranges included are 5-120 keV for ^{40}Ar , 5-70 keV for Ge, and 5-40 keV for Xe. All energy bins are 10 keV wide except for the lowest, which is 5 keV wide. Finally, we assign confidence levels to closed areas on an $\langle R_n^2 \rangle$ vs. $\langle R_n^4 \rangle$ plot by running the Monte Carlo many times and dividing the number of times the minimum- χ^2 result falls in that area by the total number of runs.

With this setup, we vary the size of the detector until the $\langle R_n^2 \rangle^{1/2}$ or $\langle R_n^2 \rangle_{\text{eff}}^{1/2}$ inside the 91% confidence region vary by only about $\pm 5\%$ from the best values. For that level of precision, 3.5 tonnes of argon are necessary, 1.5 tonnes of germanium, and 300 kg of xenon. The required detector mass decreases with atomic size because the event rate increases roughly as N^2 .

The sizes of current and proposed cryogenic detectors

can give an idea of the feasibility of this measurement. In the case of argon, the existing ICARUS T600 detector contains 500 tons of LAr [35], suggesting that a detector big enough to for measure the form factor is feasible. For germanium, existing dark-matter detectors such as CDMS II [36] consist of a few kg of germanium. The TEXONO-CDEX program is currently using a 1 kg high-purity germanium detector for neutrino physics and dark matter searches [37]. The MAJORANA [38] and GERDA [39] double-beta decay experiments will soon deploy about 40 kg of germanium enriched in ^{76}Ge . One proposed experiment, GEODM [17, 36], would be made up of 300 ~ 5 kg Ge crystals, making a total mass of ~ 1.5 tonnes. Existing xenon detectors, such as XENON100 [40] and LUX [41], are made up of on the order of a few hundred kg of xenon, approximately the amount required for a form factor measurement. A proposed experiment, the LUX-ZEPLIN project, will use 1.5 tonnes of Xe [41].

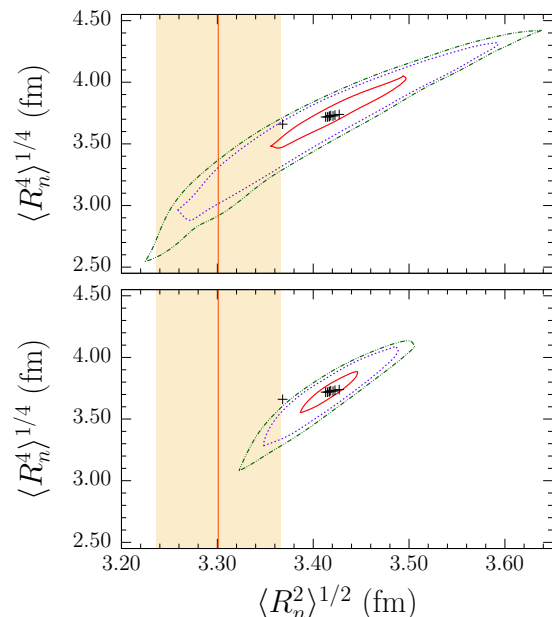


FIG. 3. Confidence regions in the $\langle R_n^2 \rangle^{1/2}$ - $\langle R_n^4 \rangle^{1/4}$ plane for an argon detector of mass 3.5 tonnes. The curves enclose confidence regions of 40%, 91%, and 97%. The colored vertical band shows the experimental result reported for the RMS radius, obtained from argon-carbon scattering, in Ref. [42], and the black crosses are the predictions of some commonly used Skyrme functionals, including the functional SkM* that we use to generate the “data.” Numerical results are summarized in tables III and IV. Top panel: the neutrino flux is allowed to vary by $\pm 10\%$. Bottom panel: the flux is assumed to be known exactly.

The results of the analysis appear in Figs. 3, 4, and 5. The closed curves correspond to 40% confidence, 91% confidence, and 97% confidence. As mentioned above, we considered two cases: one in which the normalization of the flux is allowed to vary (by $\pm 10\%$), and a second in which the normalization is kept constant. The

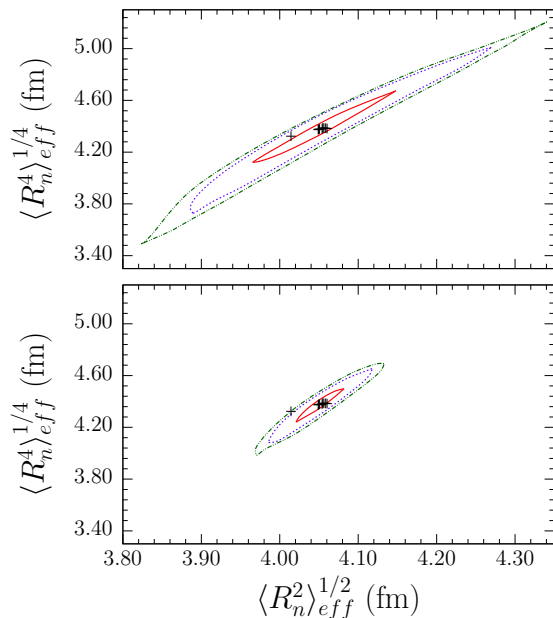


FIG. 4. Same as Fig. 3, but for effective moments in germanium, and without experimental result.

top panels of each figure show the results with the flux unconstrained within that 10% range, and the bottom panels show the same results with the assumption that the flux is known perfectly. The colored vertical band in Fig. 3 shows a model-dependent experimental result for the RMS radius, obtained from argon-carbon scattering

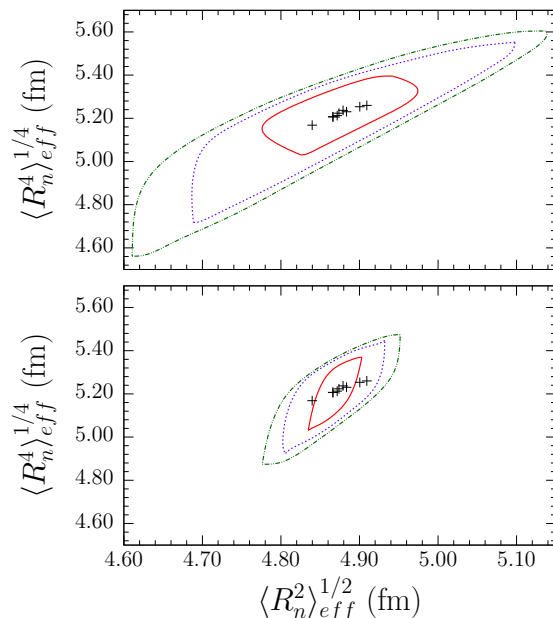


FIG. 5. Same as Fig. 4, but in xenon.

in Ref. [42]. There is a clear discrepancy between that result and the predictions of the 9 Skyrme functionals selected for this study, labeled by small crosses in Fig. 3 (the outlier in Figures 3-4 corresponds to the SkX functional of [25], which predicts systematically smaller radii than other functionals). Those functionals include SkM*, the one we use to generate the “data.” This discrepancy is mentioned by Ozawa *et al.*, but no explanation is offered. While we marginalize over $\langle R_n^6 \rangle_{eff}$ for xenon, the quantity is poorly constrained and not included in the plot in Fig. 5. Numerical results at the 91% confidence level for the mean, minimum, and maximum of the (effective) RMS neutron radius and fourth moment, (and sixth moment in xenon) appear in Tabs. III and IV.

B. Discussion

There are several noticeable differences among figures 3, 4, and 5. The first is the dependence on $\langle R_n^4 \rangle_{eff}^{1/4}$. For ^{40}Ar , the range of plausible values is large compared to the range of $\langle R_n^2 \rangle_{eff}^{1/2}$. As the nuclei grow in size to germanium and then xenon, the range of $\langle R_n^4 \rangle_{eff}^{1/4}$ gets smaller. In germanium and xenon, it is comparable to the range of the effective RMS neutron radius.

We can explain this difference by isolating the effects of the (effective) fourth moment on the recoil distributions. In ^{40}Ar , a 10% change in the fourth moment results in approximately 0.2% more events, as compared to the 1.2% difference with a 10% change in the RMS radius. In comparison, the same change in $\langle R_n^4 \rangle_{eff}^{1/4}$ of 10% results in 1.3% and 3% more events for germanium and xenon, respectively, as compared to 6% and 8% from a 10% change in $\langle R_n^2 \rangle_{eff}^{1/2}$. The nuclear recoil energy at which this difference is concentrated decreases and the importance of the fourth moment relative to the RMS radius increases as the nuclear mass increases.

Our ability to learn about the nuclear quantities $\langle R_n^2 \rangle_{eff}^{1/2}$ and $\langle R_n^4 \rangle_{eff}^{1/4}$ obviously improves if we can get an independent handle on the beam normalization. This can be seen clearly by comparing the top and bottom panels in Figs. 3, 4 and 5. The range in $\langle R_n^2 \rangle_{eff}^{1/2}$ in all three elements shrinks to $\pm 2\%$ at the 91% level in the bottom panels, where the beam normalization is known exactly. Likewise, the range in $\langle R_n^4 \rangle_{eff}^{1/4}$ decreases for all three elements. The effect is most dramatic for ^{40}Ar , where the uncertainty decreases to $\sim \pm 10\%$, but it exists in both germanium and xenon as well.

As mentioned above, we consider the systematic error of the uncertainty in detection efficiency. In order to study the effect, we remove the statistical error and randomly distribute systematic errors, proportional to the number of events in the bin, at the level of 10%, 1% and 0.1% in each bin in an uncorrelated manner. At the 10% level, detectors of the size considered here lose the ability to make any useful measurement of the neutron radius. When we lower the uncertainty in detection efficiency to

TABLE III. Numerical results at the 91% confidence level for the 3.5 tonne ^{40}Ar detector, the 1.5 tones Ge detector, and the 300 kg Xe detector with L_ν allowed to vary by $\pm 10\%$. The first column contains the element, the second the moment or effective moment considered in the corresponding row, the third the calculated values of the moments or effective moments for the Skyrme model SkM*, the fourth the mean values for the moments or effective moments, produced by the Monte Carlo, the fifth the percent difference between the mean values and the SkM* values, the sixth the minimum values chosen by the Monte Carlo, and the seventh the percent difference between the minimum and the mean value. The eighth column gives the maximum values chosen by the Monte Carlo, and the ninth column gives the percent difference between the maximum and the mean values.

		SkM* values	Mean	% Difference (from SkM*)	Min	% Difference (from mean)	Max	% Difference (from mean)
^{40}Ar	$\langle R_n^2 \rangle^{1/2}$ (fm)	3.4168	3.4103	-0.2	3.2587	-4	3.5999	+6
	$\langle R_n^4 \rangle^{1/4}$ (fm)	3.7233	3.6576	-2	2.8304	-23	4.3210	+18
Ge	$\langle R_n^2 \rangle_{\text{eff}}^{1/2}$ (fm)	4.0495	4.0516	+0.05	3.8792	-4	4.2697	+5
	$\langle R_n^4 \rangle_{\text{eff}}^{1/4}$ (fm)	4.3765	4.3603	-0.4	3.7276	-15	5.0096	+15
Xe	$\langle R_n^2 \rangle_{\text{eff}}^{1/2}$ (fm)	4.8664	4.8648	-0.001	4.6788	-4	5.0980	+5
	$\langle R_n^4 \rangle_{\text{eff}}^{1/4}$ (fm)	5.2064	5.1914	-0.3	4.7180	-10	5.5521	+7
	$\langle R_n^6 \rangle_{\text{eff}}^{1/6}$ (fm)	5.4887	5.3149	-3	0.5491	-90	10.433	+97

TABLE IV. Same as table III, except for L_ν held constant.

		SkM* values	Mean	% Difference (from SkM*)	Min	% Difference (from mean)	Max	% Difference (from mean)
^{40}Ar	$\langle R_n^2 \rangle^{1/2}$ (fm)	3.4168	3.4154	-0.04	3.3483	-2	3.4933	+2
	$\langle R_n^4 \rangle^{1/4}$ (fm)	3.7233	3.7018	-0.6	3.2826	-11	4.0865	+10
Ge	$\langle R_n^2 \rangle_{\text{eff}}^{1/2}$ (fm)	4.0495	4.0491	-0.009	3.9857	-1.6	4.1175	+1.7
	$\langle R_n^4 \rangle_{\text{eff}}^{1/4}$ (fm)	4.3765	4.3679	-0.2	4.0826	-7	4.6546	+7
Xe	$\langle R_n^2 \rangle_{\text{eff}}^{1/2}$ (fm)	4.8664	4.8654	-0.02	4.7958	-1.4	4.9323	+1.4
	$\langle R_n^4 \rangle_{\text{eff}}^{1/4}$ (fm)	5.2064	5.1990	-0.14	4.9265	-5	5.4478	+5
	$\langle R_n^6 \rangle_{\text{eff}}^{1/6}$ (fm)	5.4887	5.3877	-1.8	0.5491	-90	10.433	+94

1%, measurements of the neutron radius to $\sim \pm 5\text{-}7\%$ are possible. At this level, the range in the value of the fourth moment is $\sim \pm 20\%$. If we lower the uncertainty in detector efficiency to 0.1%, the neutron radius can be measured to better than $\sim \pm 1\%$, and the fourth moment to $\pm 2\%$.

IV. CONCLUSIONS

Neutron radii are not only of fundamental interest for nuclear structure but are also needed to fully analyze supernova-neutrino signals [13] and interpret measurements of the Weinberg angle or of neutrino magnetic moments [14]. At present the distributions of neutrons in nuclei is not known nearly as well as those of protons.

We have presented a model-independent method, involving the Taylor expansion of the scattering form factor, for extracting the RMS radius and fourth moment of the neutron density distribution in certain nuclei from the nuclear-recoil distribution in a neutrino-scattering experiment. The radius and fourth moment can also be cal-

culated theoretically, so that our technique will provide a straightforward connection between theory and experiment. To obtain a rough estimate of the effectiveness of this approach, we considered a stopped pion neutrino source of 3×10^7 neutrinos/cm²/s and liquid Ar, Ge, and Xe detectors in the tonne range. We conclude that it is possible to determine the neutron radius to a few percent if the uncorrelated error on the efficiency is less than 1%. The detailed analysis of the shape of the recoil spectrum in a cryogenic detector, such as the one we have suggested here, has not previously been considered. More detailed simulations of realistic experimental setups are therefore required for definitive feasibility studies.

V. ACKNOWLEDGEMENTS

We thank Kate Scholberg for helpful discussions. This work was supported by a GAANN fellowship (KP), by DOE contract DE-FG02-02ER41216 (KP and GM), by DOE Contract DE-FG02-97ER41019 (JE). It was partly performed under the auspices of the US Department of

Energy by the Lawrence Livermore National Laboratory under Contract DE-AC52-07NA27344, and funding was also provided by the United States Department of Energy Office of Science, Nuclear Physics Program pursuant to

Contract DE-AC52-07NA27344 Clause B-9999, Clause H-9999 and the American Recovery and Reinvestment Act, Pub. L. 111-5 (NS).

-
- [1] M. Bender, P.-H. Heenen, and P.-G. Reinhard, *Rev. of Mod. Phys.* **75**, 121 (2003).
 - [2] K. Kortelainen, T. Lesinski, J. Moré, W. Nazarewicz, J. Sarich, N. Schunck, M. Stoitsov, and S. Wild, *Phys. Rev. C* **82**, 24313 (2010).
 - [3] K. Kortelainen, J. McDonnell, W. Nazarewicz, P.-G. Reinhard, J. Sarich, N. Schunck, M. Stoitsov, and S. Wild, *Phys. Rev. C* **85**, 024304 (2012).
 - [4] P.-G. Reinhard and W. Nazarewicz, *Phys. Rev. C* **81**, 051303(R) (2010).
 - [5] F. Fattoyev and J. Piekarewicz, *Phys. Rev. C* **82**, 025810 (2010).
 - [6] B.-A. Li and A. Steiner, *Phys. Lett. B* **642**, 436 (2006).
 - [7] A. W. Steiner, J. M. Lattimer, and E. F. Brown, *Astrophys. J.* **722**, 33 (2010).
 - [8] A. W. Steiner and S. Gandolfi, *Phys. Rev. Lett.* **108** (2012).
 - [9] A. Steiner, M. Prakash, J. Lattimer, and P. Ellis, *Physical Reports* **411**, 325 (2005).
 - [10] C. Horowitz, S. Pollock, P. Souder, and R. Michaels, *Phys. Rev. C* **63**, 025501 (2001), [arXiv:nucl-th/9912038 \[nucl-th\]](#).
 - [11] S. Abrahamyan *et al.* (PREX Collaboration), *Phys. Rev. Lett.* , 112502.
 - [12] P. Amanik and G. McLaughlin, *J. Phys. G* **36**, 015105 (2009).
 - [13] C. J. Horowitz, K. Coakley, and D. McKinsey, *Phys. Rev. D* **68**, 023005 (2003), [arXiv:astro-ph/0302071 \[astro-ph\]](#).
 - [14] K. Scholberg, *Phys. Rev. D* **73**, 033005 (2006), [arXiv:hep-ex/0511042 \[hep-ex\]](#).
 - [15] A. Bueno, M. C. Carmona, J. Lozano, and S. Navas, *Phys. Rev. D* **74**, 033010 (2006).
 - [16] J. A. Formaggio, E. Figueroa-Feliciano, and A. Anderson, (2011), [arXiv:1107.3512 \[hep-ph\]](#).
 - [17] A. Anderson, J. Conrad, E. Figueroa-Feliciano, K. Scholberg, and J. Spitz, *Phys. Rev. D* **84**, 013008 (2011), [arXiv:1103.4894 \[hep-ph\]](#).
 - [18] J. Barranco, O. G. Miranda, and T. I. Rashba, *J. of High Energy Phys.* **12**, 21 (2005).
 - [19] J. Bartel, P. Quentin, M. Brack, C. Guet, and H.-B. Håkansson, *Nucl. Phys. A* **386**, 79 (1982).
 - [20] D. McKinsey and K. Coakley, *Astroparticle Physics* **22**, 355 (2005).
 - [21] K. Scholberg, T. Wongjirad, E. Hungerford, E. A., D. Markoff, P. Mueller, Y. Efremenko, D. McKinsey, and J. Nikkel, *Proceedings of the DPF-2009 Conference* (2009), [arXiv:hep-ex/0910.1989v2](#).
 - [22] J. K. Tuli, “Nuclear Wallet Cards,” (2008).
 - [23] P.-G. Reinhard and H. Flocard, *Nucl. Phys. A* **584**, 467 (1995).
 - [24] E. Chabanat, P. Bonche, P. Haensel, J. Meyer, and R. Schaeffer, *Nucl. Phys. A* **635**, 231 (1998).
 - [25] A. B. Brown, *Phys. Rev. C* **58**, 220 (1998).
 - [26] S. Goriely, M. Samyn, J. Pearson, and M. Onsi, *Nucl. Phys. A* **750**, 425 (2005).
 - [27] P.-G. Reinhard, D. Dean, W. Nazarewicz, J. Dobaczewski, J. Maruhn, and M. Strayer, *Phys. Rev. C* **60**, 014316 (1999).
 - [28] M. Stoitsov, N. Schunck, M. Kortelainen, N. Michel, H.-A. Nam, J. Sarich, and S. Wild, To be submitted to *Computer Physics Communications* (2012).
 - [29] N. Nikolov, N. Schunck, W. Nazarewicz, M. Bender, and J. Pei, *Phys. Rev. C* **83**, 034305 (2011).
 - [30] S. Perez-Martin and L. Robledo, *Phys. Rev. C* **78**, 014304 (2008).
 - [31] N. Schunck, J. Dobaczewski, J. McDonnell, J. Moré, W. Nazarewicz, J. Sarich, and M. Stoitsov, *Phys. Rev. C* **81**, 024316 (2010).
 - [32] J. M. Conrad (DAE δ ALUS Collaboration), (2010), [arXiv:1012.4853 \[hep-ex\]](#).
 - [33] J. M. Conrad and M. H. Shaevitz, *Phys. Rev. Lett.* **104**, 141802 (2010), [arXiv:0912.4079 \[hep-ex\]](#).
 - [34] G. Drexlin *et al.*, *Progress in Particle and Nuclear Physics* **40**, 193 (1998).
 - [35] S. Amerio *et al.*, *Nucl. Instr. Meth. A* **527**, 329 (2004).
 - [36] E. Figueroa-Feliciano (CDMS Collaboration), *AIP Conf. Proc.* **1200**, 959 (2010).
 - [37] H. T. Wong, *J. Phys.: Conf. Ser.* **309** (2011).
 - [38] D. G. Phillips II *et al.*, (2011), [arXiv:1111.5578 \[nucl-ex\]](#).
 - [39] I. Abt *et al.*, (2004), [arXiv:0404039 \[hep-ex\]](#).
 - [40] E. Aprile *et al.* (XENON100 Collaboration), *Astropart. Phys.* **35**, 573 (2012).
 - [41] D. McKinsey *et al.*, *J. Phys. Conf. Ser.* **203**, 012026 (2010).
 - [42] A. Ozawa *et al.*, *Nucl. Phys. A* **709**, 60 (2002).